



Phase transitions of harzburgite and buckled slab under eastern China

Yanfei Zhang

State Key Laboratory of Geological Processes and Mineral Resources, China University of Geosciences (Wuhan), Wuhan, China

Yanbin Wang

Center for Advanced Radiation Sources, The University of Chicago, Chicago, Illinois, USA (wang@cars.uchicago.edu)

Yao Wu

State Key Laboratory of Geological Processes and Mineral Resources, China University of Geosciences (Wuhan), Wuhan, China (ywu@cug.edu.cn)

Craig R. Bina

Department of Earth and Planetary Sciences, Northwestern University, Evanston, Illinois, USA

Zhenmin Jin

State Key Laboratory of Geological Processes and Mineral Resources, China University of Geosciences (Wuhan), Wuhan, China

Shuwen Dong

Chinese Academy of Geological Sciences, Beijing, China

[1] Phase relations in harzburgite have been determined between 14 and 24 GPa and 1473 and 1673 K. At 1673 K, harzburgite transformed to wadsleyite + garnet + clinopyroxene below 19 GPa and decomposed into an assemblage of ringwoodite + garnet + stishovite above 20 GPa. Certain amounts of akimotoite were produced at still higher pressures (22–23 GPa). Finally, perovskite and magnesiowüstite were found to coexist with garnet at 24.2 GPa. Compositions of all the phases were analyzed and elemental partitioning coefficients were determined among coexisting phases. Combining our experimental data with available thermoelastic properties of major minerals in the earth's mantle, we modeled the velocity and density signatures of the stagnated oceanic slab in the mantle transition zone (MTZ) under eastern China, based on kinematic slab thermal structure analysis. We examined two end-member slab models: a conventional straight slab with deformation thickening and an undulate slab with an oscillating wavelength of 200 km. We found that an undulated (buckled) slab model yields velocity anomalies (about 1–2% for V_p) that are consistent with seismic tomography models, taking into account low-pass filtering effects in seismic tomography studies. On the other hand, straight slab models yield velocity anomalies that are too high compared with seismic tomography models. Our models provide important constraints on the thermal structure, mineralogy, composition, density, and velocities of slab materials in the MTZ.

Components: 10,600 words, 12 figures, 4 tables.

Keywords: harzburgite; high pressure high temperature experiment; eastern China; stagnant slabs; mantle transition zone.

Index Terms: 3630 Mineralogy and Petrology: Experimental mineralogy and petrology; 3939 Mineral Physics: Physical thermodynamics; 7208 Radio Science: Mantle (1212, 1213, 8124); 7240 Seismology: Subduction zones (1207, 1219, 1240); 7270 Seismology: Tomography (6982, 8180)

Received 4 October 2012; Accepted 14 January 2013; Published 30 April 2013.

Zhang Y., Y. Wang, Y. Wu, C. Bina, Z. Jin, and S. Dong (2013), Phase transitions of harzburgite and buckled slab under eastern China, *Geochem. Geophys. Geosyst.*, 14, 1182–1199, doi:10.1002/ggge.20069.

1. Introduction

[2] Subducted materials play an important role in affecting chemical composition and structure of the mantle transition zone (MTZ). Harzburgite is generally accepted as an important part of subducting slabs, overlain by a layer of basalt and underlain by a layer of depleted peridotite (lherzolite) [Ringwood, 1982; Ringwood and Irifune, 1988]. Seismic tomography studies have detected well-developed widespread fast anomalies in the MTZ and lower mantle around the circum-Pacific, southern Europe, southern Mexico, and southern America [e.g., van der Hilst et al., 1991; Fukao et al., 1992, 2001, 2009; Zhao, 2004]. These anomalies have been interpreted as stagnant oceanic lithosphere materials as these regions are closely associated with subduction zones, where the oceanic lithosphere plunges deeply into the mantle. Under eastern China, where the Pacific oceanic lithosphere has been subducting deep into the mantle since the Late Mesozoic [Li and van der Hilst, 2010], continuous fast anomalies (1–2% faster than the surrounding mantle) are imaged at depths of ca. 500–660 km, extending from the Japan Wadati-Benioff zone to Ordos Block, over a longitude interval of nearly 30° [e.g., Huang and Zhao, 2006; Li and van der Hilst, 2010; Pei and Chen, 2010]. P-wave triplication studies have also detected a high-velocity and low-gradient layer between ~600 and 660 km, with maximum anomalies about 2–3% higher than the global average P-wave velocity at these depths [Tajima et al., 2009; Wang and Chen, 2009; Wang and Niu, 2010]. Receiver-function imaging studies show complex discontinuity structures in the lower part of MTZ, with transition zone thicknesses about 30–40 km greater than the global average [e.g., Ai et al., 2003; Chen and Ai, 2009]. These are also thought to be closely related to subducted Pacific lithosphere.

[3] Fast anomalies can be induced by low temperature, different composition/mineralogy, or a combination of both. Driven by gravitational forces, these thermal and/or compositional heterogeneities either float or sink through the mantle, facilitating thermal and chemical exchanges therein. Systematic experimental studies on slab materials at high pressure and high temperature (HPHT) are crucial in testing the stagnant slab hypothesis and providing

quantitative constraints on thermal structure, mineralogy, composition, density, and velocities of slab materials in the deep mantle. However, previous HPHT experiments mainly focused on phase transitions of basalt [e.g., Irifune and Ringwood, 1987a, 1993; Hirose et al., 1999; Sanehira et al., 2008]; few reports on harzburgite are available [Irifune and Ringwood, 1987b]. By using a “harzburgite minus olivine” composition, Irifune and Ringwood [1987b] reported the phase relation of the residuum, but the interaction between “olivine normative component” and “pyroxene normative component” has been ignored in their study.

[4] In this study, we conducted HPHT experiments on a natural harzburgite at 1473–1673 K and 14.1–24.2 GPa. We first investigated mineralogy of subducted harzburgite under pressure and temperature conditions corresponding to the MTZ. Combining the experimental data with available thermoelastic properties of the high-pressure minerals and kinematic slab thermal structure analysis, we next examined velocity and density signatures of stagnated slabs. By comparing our results with seismic tomography studies, we evaluated thermodynamic and mechanical states of stagnated slabs in the MTZ under eastern China.

2. Experiment Procedures

2.1. Starting Materials

[5] The harzburgite starting material was synthesized by mixing approximately 82 wt % olivine with 18 wt % enstatite. Both minerals were hand-picked from a natural peridotite sample (DMP-018) from Damaping (Hannuoba), Hebei Province, China. For detailed description of the geological setting and the sample, see Liu et al. [2005a] and Wang et al. [2010]. The olivine and enstatite crystals were first crushed and ground into fine powder (grain size 5–15 μm) separately, then ground together in alcohol with an agate mortar to produce a homogeneous mix. The chemical composition of the harzburgite (Table 1) thus prepared is similar to that from North Atlantic [Michael and Bonatti, 1985] and East Pacific Rise [Dick and Natland, 1996]. Compared with pyrolite, harzburgite is generally lower in alumina and calcia but higher

Table 1. Compositions of Harzburgite Used in this Study and Previous Work

	Pyrolite	North Atlantic	East Pacific	This study	Harzburgite minus olivine
SiO ₂	45.0	43.64	43.3	43.86	52.95
TiO ₂	0.20	0.01	0.03	0.04	0.19
Al ₂ O ₃	4.45	0.65	0.41	0.72	4.15
Cr ₂ O ₃	0.38	0.53	0.18	0.06	2.89
FeO	8.05	7.83	8.4	9.23	5.87
MgO	37.8	46.36	47	45.46	31.01
CaO	3.55	0.5	0.45	0.08	2.79
Na ₂ O	0.36	0.01	0	0.01	0.09
MnO	0.14	0	0.12	0.14	0
NiO	0.25	0	0.26	0	0
Total	100.18	99.53	100.15	99.6	99.94

Pyrolite: *McDonough and Sun* [1995]. North Atlantic: harzburgite from North Atlantic, *Michael and Bonatti* [1985]. East Pacific: harzburgite from East Pacific, *Dick and Natland* [1996]. Harzburgite minus olivine: *Irifune and Ringwood* [1987b].

in magnesia. The starting material used by *Irifune and Ringwood* [1987b], a “harzburgite minus 82 wt % olivine” composition consisting mainly of enstatite with minor amount of spinel (MgAl₂O₄), is also shown in Table 1 for comparison. Water content of the starting material was measured by FT-IR spectroscopy using the method of *Bell et al.* [1995, 2003], yielding about 60 ppm (by weight) H₂O in enstatite and no water in olivine. Water contents in the run products could not be measured reliably as crystal sizes were too small.

2.2. High-Pressure, High-Temperature Experiments

[6] HPHT experiments were carried out in a 1000-ton Kawai-type multi-anvil apparatus at the Laboratory for Study of the Earth’s Deep Interior (SEDI Lab), China University of Geosciences (Wuhan). Cell assemblies, with 10 and 8 mm octahedral edge lengths and 5 and 3 mm truncation edge lengths (TEL), respectively (hereafter referred to as the 10/5 and 8/3 assemblies, respectively; Figure 1), were used on 25.4 mm edge-length WC cubes. The octahedral pressure media were made by injection-molded polycrystalline spinel, as developed by *Leinenweber et al.* [2012] in a project supported by the Consortium for Materials Properties Research in Earth Sciences to develop standardized high-pressure assemblies for various conditions. A LaCrO₃ sleeve was placed inside of the spinel octahedron for thermal insulation. A rhenium furnace was used for heating. The sample, contained in a Re capsule, was insulated from the furnace by an alumina inner capsule. Type C W-Re thermocouple was used to measure the temperature at the center of furnace.

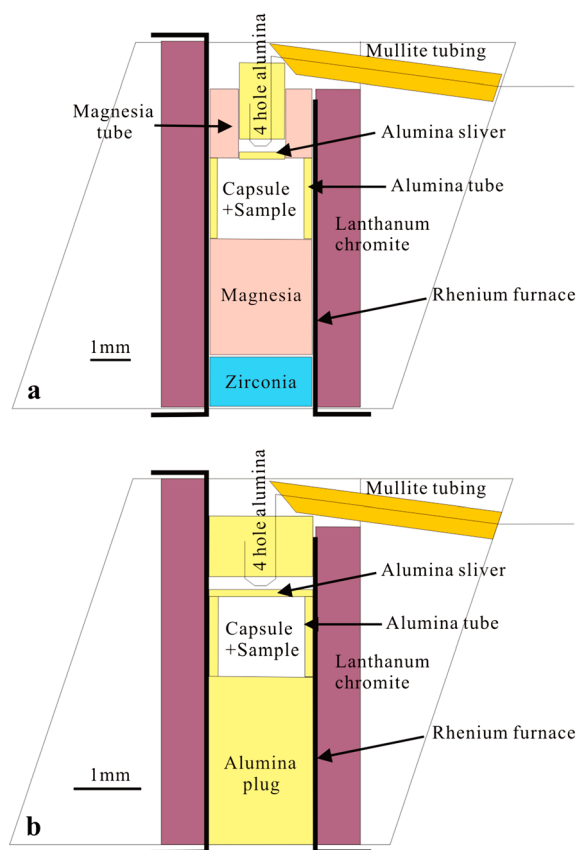


Figure 1. Schematic cross sections of the cell assemblies used in this study. (a) The 10/5 assembly. (b) The 8/3 assembly [*Leinenweber et al.*, 2012].

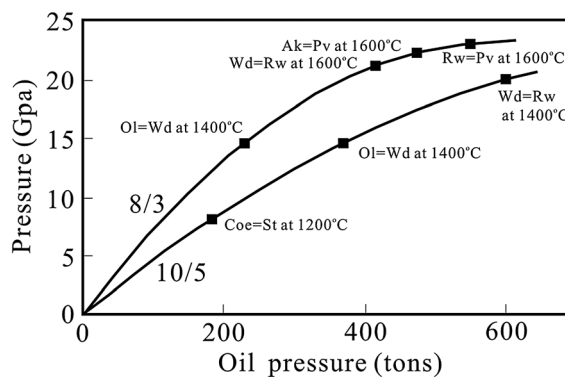


Figure 2. Pressure calibration curves at high temperatures for the 10/5 and 8/3 assemblies. Temperature effects on pressure generation are negligible.

Typical temperature variation during the experiments was within $\pm 10^\circ\text{C}$, without correcting for the pressure effect on electromotive force.

[7] Figure 2 shows the pressure calibration curves used in the present study. For the 10/5 assembly (Figure 1a), high-temperature pressure calibration was performed using the olivine-wadsleyite (14.6

GPa [Katsura and Ito, 1989; Fei and Bertka, 1999; Katsura et al., 2004]) and wadsleyite-ringwoodite transitions (20 GPa [Katsura and Ito, 1989; Suzuki et al., 2000]) in Mg_2SiO_4 at 1673 K, as well as the phase transition of coesite-stishovite in SiO_2 at 1473 K (9.2 GPa [Zhang et al., 1996]). For details of the cell assembly and pressure calibration see Wu et al. [2011]. For the 8/3 assembly (Figure 1b), pressure calibration was made according to the olivine-wadsleyite transition (14.6 GPa [Katsura and Ito, 1989; Fei and Bertka, 1999; Katsura et al., 2004]) in Mg_2SiO_4 at 1673 K, wadsleyite-ringwoodite (21.3 GPa [Suzuki et al., 2000]) and the ringwoodite to perovskite+periclase transformations (23.1 GPa [Fei et al., 2004]) in Mg_2SiO_4 and akimotoite-perovskite in $MgSiO_3$ (22.3 GPa [Hirose et al., 2001; Fei et al., 2004]), all at 1873 K. The calibration curves appear temperature independent between 1473 and 1873 K, and reproducibility of pressure in the present experiments was estimated to be about ± 0.3 GPa and ± 0.5 GPa, respectively, for the 10/5 and 8/3 assemblies.

[8] Prior to each experiment, the cell assembly, with samples loaded, was dried at 393 K for 24 h in an oven. In all experiments, the samples were first compressed to the desired ram load, then heated at a rate of ~ 100 K/min and held at the constant target temperature for the desired duration, which varied from 5 to 24 h. Each experiment was terminated by switching off power to the furnace (quenching), followed by automatic decompression to atmospheric pressure at a rate of about -1.0 GPa/h. After recovery, the Re capsule containing the samples was mounted in a plastic ring filled with

epoxy resin and polished for phase identification and compositional analysis.

2.3. Analysis of Run Products

[9] Microfocus X-ray diffraction (X'Pert PRO DY2198) was used to identify phases in the recovered run products. A field-emission scanning electron microscope (Quanta 2000-type) (FE-SEM), fitted with a LINK EDS detector, was used to study microstructure of the recovered samples. Quantitative composition analyses were conducted with an electron probe microanalyzer (EPMA-1600) at the University of Science and Technology of China, using an accelerating voltage of 15 kV, a beam size of $1.0 \mu m$, and a beam current of 20 nA. General measurement errors are about 3% for elements of less than 1 wt %, 1 % for elements of less than 5 wt %, and 0.1 % for elements of greater than 10 wt %.

3. Experiment Results

[10] Figure 3 shows X-ray diffraction profiles of representative experiments. Details of the experimental conditions and run products are summarized in Table 2. Figure 4 shows representative back-scattered electron images of typical run products. Mineral proportions were calculated based on mass balance. Chemical compositions and densities of minerals, listed in Tables 3 and 4, were used to determine the volume fractions (vol%) of minerals in harzburgite (Table 2 and Figure 5). It can be seen that the effect of temperature on the phase proportion is negligible between 1473 and 1673 K.

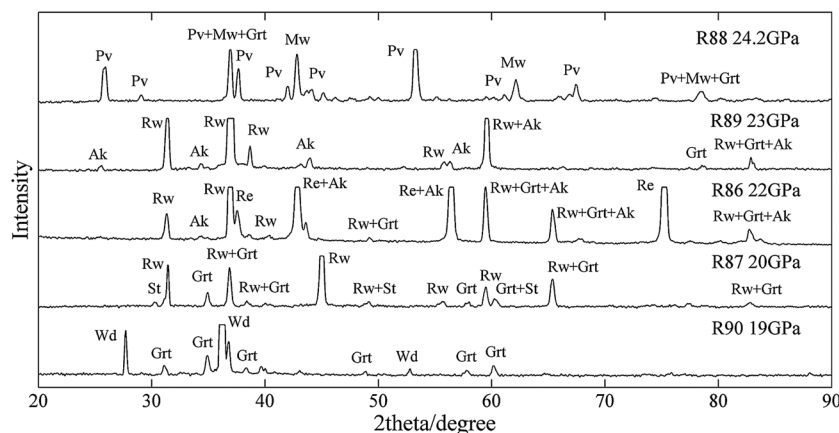


Figure 3. X-ray diffraction profiles of representative run products at 1673 K. Mineral abbreviations: Ol, olivine; Wd, Wadsleyite; Grt, garnet; Cpx, clinopyroxene; Rw, ringwoodite; Ak, akimotoite; St, stishovite; Pv, perovskite; Mw, magnesiowüstite; Re, rhenium (capsule).

Table 2. Summary of Experimental Conditions and Run Products

Run no.	Pressure (GPa)	Temperature (K)	Assembly	Duration (h)	Phases
R64	14.1	1673	10/5	6	Wd (40) + Ol (43) + Grt (6) + Cpx (11)
R68	15.1	1673	10/5	6	Wd + Grt + Cpx
R71	16.1	1673	10/5	6	Wd (83) + Grt (7) + Cpx (10)
R90	19	1673	8/3	5	Wd (83) + Grt (17)
R87	20	1673	8/3	6	Rw (88) + Grt (10) + St (2)
R86	22	1673	8/3	6	Rw (83) + Grt (7) + Ak (10) + tr.St
R89	23	1673	8/3	6	Rw (82) + Grt (16) + Ak (2)
R88	24.2	1673	8/3	6	Pv (59) + Mw (29) + Grt (12)
R95	18	1473	8/3	24	Rw (87) + Grt (12) + St (1)
R92	19	1473	8/3	24	Rw (87) + Grt (12) + St (1)
R93	20	1473	8/3	24	Rw (87) + Grt (12) + St (1)
R97	22	1473	8/3	24	Rw (86) + Grt (12) + St (2) + tr.Ak
R98	24	1473	8/3	24	Rw + Pv + Mw + Grt

Abbreviations: Ol, olivine; Wd, wadsleyite; Grt, garnet; Cpx, clinopyroxene; Rw, ringwoodite; St, stishovite; Ak, akimotoite; Pv, perovskite; Mw, magnesiowüstite.

[11] For experiments below 16.1 GPa, granular and columnar garnet crystals formed with grain size about 1–5 μm , inside former clinopyroxene crystals (Figure 4a). Wadsleyite grains exhibited well-developed triple-junctions and concordant relationships with garnet and clinopyroxene crystals (Figure 4b), suggesting that equilibrium was reached. The volumetric proportion of garnet increased significantly with pressure until 19 GPa (Figure 5). Between 20 and 22 GPa, small (<1 μm), needle-like stishovite crystals formed within large garnet grains, in association with ringwoodite (Figure 4c). The exsolution of stishovite from garnet resulted in an abrupt increase in ringwoodite volume fraction between 20 and 22 GPa (Figure 5). The small crystal size of stishovite in garnet matrix is a consequence of exsolution reaction in garnet and should not be considered as evidence of disequilibrium. Preferred orientations of the stishovite “needles” are a potential source of seismic anisotropy for a deformed slab, although we did not find systematic lattice preferred orientation of stishovite in our quasi-hydrostatic experiments. When pressure increased to 22–23 GPa, granular and short columnar akimotoite polycrystalline aggregates, similar to those found in the shocked-metamorphosed Tenham chondrite [Tomioaka and Fujino, 1999], were observed to be in contact with ringwoodite (Figure 4d and e), accompanied by the disappearance of stishovite (Figure 5). The volume fraction of akimotoite decreased with increasing pressure. At 24.2 GPa, perovskite and magnesiowüstite were formed together with majoritic garnet (Figure 4f). The perovskite + magnesiowüstite assembly shows a typical texture after disproportionation reaction from ringwoodite and is virtually identical to that reported previously [Yamazaki *et al.*, 2009]. Here again, the

fine grain size should not be considered as evidence of disequilibrium. Because of the small grain size, however, reliable elemental partitioning information could be obtained only in areas where different minerals in contact were large enough to yield accurate chemical composition analysis. Results of the analyses of major minerals are given in Table 3.

[12] Figure 6a illustrates compositional changes in the olivine-normative component (olivine, wadsleyite, and ringwoodite) as a function of pressure at 1673 K. Fe preferentially partitions into wadsleyite at 14.1 GPa when olivine and wadsleyite coexist. Figure 6b shows compositional variation of garnet (oxygen number assumed to be 12) with pressure. Both Al and Fe contents decrease with pressure, while Si and Mg contents increase during the transformation from olivine to wadsleyite. Between 19 and 20 GPa, Si content drops and that of Al increases due to the wadsleyite-ringwoodite transformation and the formation of stishovite. With the formation of akimotoite at 22–23 GPa, cation numbers of Mg, Fe, and Al decrease with an increase of Si.

[13] Figure 6c shows iron partition coefficients between the olivine- and the pyroxene-normative components (clinopyroxene, garnet, and akimotoite) at 1673 K as a function of pressure. Here the partition coefficient of Mg and Fe between two phases α and β is defined by $K^{z/\beta} = (X_{\text{Fe}}/X_{\text{Mg}})^{\alpha} / (X_{\text{Fe}}/X_{\text{Mg}})^{\beta}$, where $X_{\text{Fe}} = \text{Fe}^{\text{total}} / (\text{Mg}^{2+} + \text{Fe}^{\text{total}})$. Below 14.1 GPa, Fe partitions preferentially into garnet and olivine, relative to olivine and clinopyroxene, respectively. Between 16 and 19 GPa, Fe partitions roughly equally between wadsleyite and garnet, while clinopyroxene becomes Fe-poor relative to wadsleyite by a factor of ~ 2 . These values are generally in accordance with earlier experimental results for a pyrolite system under

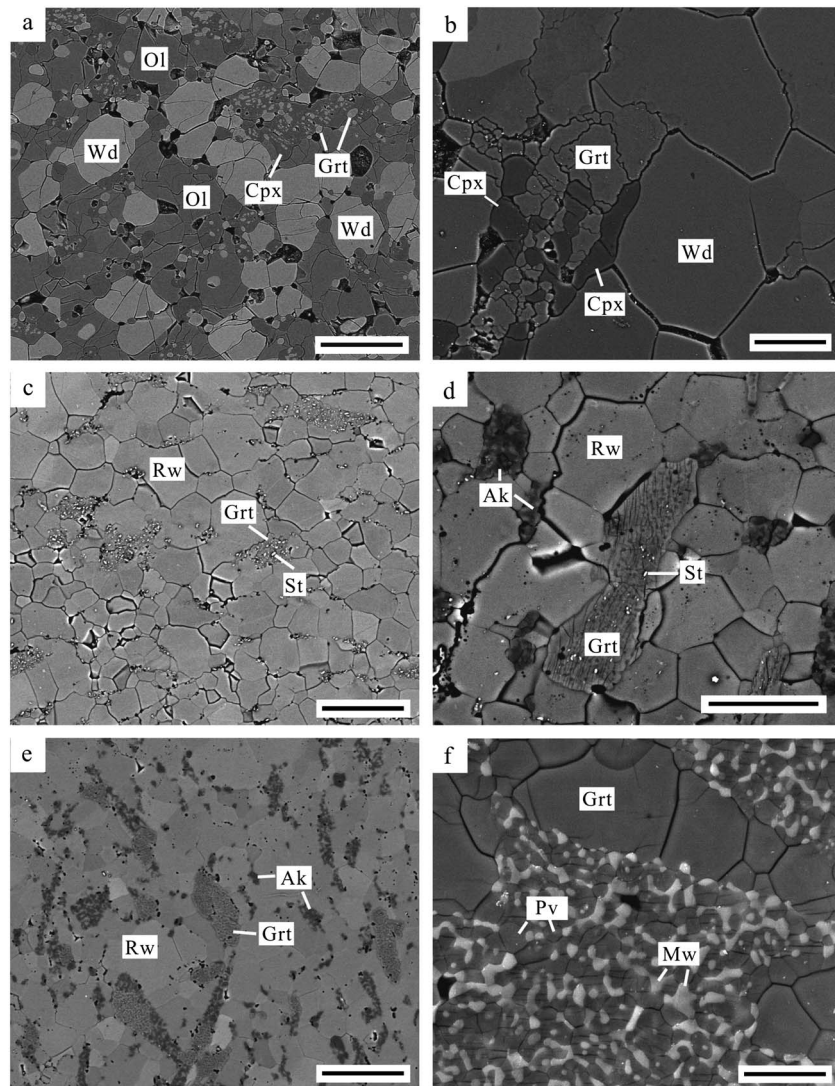


Figure 4. Microstructure of representative run products at 1673 K. (a) R64, 14.1 GPa 1673 K, scale bar: 50 μm . (b) R71, 16.1 GPa 1673 K, scale bar: 10 μm . (c) R87, 20 GPa 1673 K, scale bar: 50 μm . (d) R86, 22 GPa 1673 K, scale bar: 20 μm . (e) R89, 23 GPa 1673 K, scale bar: 50 μm . (f) R88, 24.2 GPa 1673 K, scale bar: 10 μm . Abbreviations: Ol, olivine; Wd, wadsleyite; Rw, ringwoodite; Cpx, clinopyroxene; Grt, garnet; Ak, akimotoite; St, stishovite; Pv, perovskite; Mw, magnesiowüstite.

similar conditions [Irfune and Isshiki, 1998]. After wadsleyite transforms to ringwoodite, $K^{\text{Rw/Grt}}$ increases from ca. 1.0 to 1.5 at 20–23 GPa, while $K^{\text{Rw/Ak}}$ decreases from ca. 2.9 to about 2.1 at 22–23 GPa. With increasing pressure, Fe content in akimotoite increases relative to ringwoodite, while volume fraction of akimotoite decreases (Figure 5), consistent with previous experimental studies [Ito and Yamada, 1982] and thermodynamic calculation [Fabrichnaya, 1995] on the (Mg,Fe)SiO₃ system. These consistencies suggest that equilibrium was achieved in the present experiments. One previous study [Irfune and Ringwood, 1987b], using a harzburgite-minus-olivine composition, reported

that volume fraction of akimotoite increases with increasing pressure. We attribute this discrepancy to the interactions between the olivine and non-olivine components: in the “residuum” composition of *Irfune and Ringwood* [1987b], such interactions are absent. Increasing Fe content may be a factor controlling volume fraction of akimotoite. With the formation of stishovite and akimotoite, CaSiO₃ perovskite should appear according to mass balance and Ca partition data. The amount is small (<0.1 vol.%) and therefore not shown in Figure 5.

[14] Partition coefficients of Al between akimotoite and garnet is defined by $K^{\text{Al}} = \text{Ak}^{(\text{Al}+\text{Cr})/(\text{Si}+\text{Ti})}/$

Table 3. Electron Microprobe Analyses of Representative Phases Present in the Run Products

	SiO ₂	TiO ₂	Al ₂ O ₃	Cr ₂ O ₃	FeO	MnO	MgO	NiO	CaO	Na ₂ O	Total
R64, 14.1 GPa, 1673 K, 6 h											
Wd	41.21	0.01	0.25	0.07	13.17	0.12	45.14	0.41	0.01	-	100.39
Ol	42.25	-	0.04	-	6.57	0.08	50.40	0.17	0.04	-	99.55
Grt	50.35	0.03	9.08	0.27	8.21	0.25	29.60	0.06	1.40	0.02	99.27
Cpx	59.17	0.01	0.13	0.01	3.77	0.10	35.76	0.09	0.15	0.02	99.21
R71, 16.1 GPa, 1673 K, 6 h											
Wd	41.63	0.04	0.10	0.05	9.09	0.09	47.77	0.22	0.02	-	99.01
Grt	54.46	-	4.09	0.23	6.37	0.34	32.06	-	1.25	0.04	98.84
Cpx	59.32	0.02	0.06	0.02	3.48	0.09	37.00	0.06	0.13	-	100.18
R90, 19 GPa, 1673 K, 5 h											
Wd	42.17	0.01	0.09	0.01	9.24	0.11	48.73	0.35	0.02	0.02	100.75
Grt	54.79	0.08	3.93	0.26	6.66	0.20	32.62	0.08	1.11	0.04	99.77
R86, 22 GPa, 1673 K, 6 h											
Rw	40.69	0.01	0.04	-	10.18	0.10	47.86	0.44	0.01	-	99.33
Grt	51.88	0.05	4.12	0.25	5.57	0.26	36.57	0.12	1.06	0.04	99.92
Ak	58.21	0.04	1.32	0.18	2.73	0.10	36.70	0.04	0.20	-	99.52
R89, 23 GPa, 1673 K, 6 h											
Rw	41.75	-	0.04	-	9.69	0.09	47.90	0.39	-	0.03	99.89
Grt	55.07	0.04	2.79	0.21	5.01	0.19	35.80	0.03	0.55	0.06	99.75
Ak	56.07	0.03	2.99	0.14	3.51	0.20	36.75	0.10	0.73	0.06	100.58
R95, 18 GPa, 1473 K, 24 h											
Rw	41.13	-	0.01	-	9.21	0.12	47.58	0.27	0.12	0.01	98.45
Grt	55.77	0.01	2.77	0.17	6.24	0.17	32.85	0.17	0.40	0.01	98.56
R92, 19 GPa, 1473 K, 24 h											
Rw	41.38	-	0.03	0.03	9.28	0.09	48.12	0.28	-	-	99.21
Grt	55.83	0.05	5.17	0.32	5.98	0.31	30.90	0.09	1.05	0.05	99.75
R97, 22 GPa, 1473 K, 24 h											
Rw	41.13	-	0.02	0.01	9.67	0.07	48.15	0.29	-	0.02	99.36
Grt	54.38	0.06	4.28	0.21	5.68	0.34	32.72	0.16	0.93	0.08	98.84
Ak	56.71	0.16	2.11	0.16	4.45	0.17	33.69	0.16	0.34	0.02	97.97

Mineral abbreviations are same as in Figure 4.

$\text{Grt}^{(\text{Al}+\text{Cr})/(\text{Si}+\text{Ti})}$, and the results are also shown in Figure 6c (vertical axis to the right). K^{Al} increases from ~0.3 to ~1.0. At low pressures, Al partitions almost exclusively into garnet. Partitioning measurements on Ca have large uncertainties because Ca content is low in harzburgite (<0.5 wt %). These data are therefore not presented.

[15] The interaction between the olivine- and pyroxene-normative components is primarily through partitioning of Fe on the Mg site in the phases involved [Weidner and Wang, 2000]. It can be seen from Figure 6c that the partition of Fe between wadsleyite, ringwoodite, and garnet changes very little, indicating that the interaction between olivine- and pyroxene-normative components has little effect on the transformation of wadsleyite to ringwoodite. Between 20 and 22 GPa, the formation of stishovite and akimotoite affects the ringwoodite-versus-garnet proportion significantly in harzburgite and

will cause detectable changes in seismic velocities and density (to be discussed below).

4. Mineral Physics Analysis on Subducted Lithospheric Materials in the MTZ

4.1. Buoyancy Relationship of Harzburgite Relative to a Pyrolytic Mantle

[16] We used the third-order high-temperature Birch-Murnaghan equation of state to calculate densities of minerals at high-temperature and high-pressure conditions. Procedures used for the calculation along the subduction geotherm were the same as that of Irifune and Ringwood [1987b]. Thermodynamic parameters of major minerals listed in Table 4 are used to calculate densities of harzburgite and pyrolyte (Figure 7a), as well as basalt at various high-pressure and high-temperature conditions. Phase

Table 4. Thermoelastic Parameters of Major Mantle Minerals

	Olivine	Wadsleyite	Ringwoodite	Hp-Cen	Garnet
ρ (g/cm ³)	3.222+ 1.182* XFe ^[c]	3.472+ 1.24* XFe ^[c]	3.548+ 1.3* XFe ^[c]	3.304+0.826* XFe ^[m,aa]	3.512+0.8*XFe+0.09* XCa ^[ab]
K _{So} (GPa)	130 ^[a,b,d,e]	173 ^[g,h,i]	185 ^[j,k]	157* ^[m]	168 ^[o,p,q]
K _{So'}	4.6 ^[b]	4.5 ^[g,h,i]	4.5 ^[j,k]	5.6* ^[m]	4.1 ^[p,u]
$\partial K_S/\partial T$ (GPa/K)	-0.016 ^[b]	-0.012 ^[g,i]	-0.021 ^[c,k]	-0.017* ^[m]	-0.015 ^[o]
G ₀ (GPa)	77 ^[a,b,d,e]	113 ^[g,h,i]	120 ^[j,k]	99* ^[m]	88 ^[n,o,p,q]
G _{0'}	1.6 ^[b,e]	1.5 ^[g,h,i]	1.5 ^[j,k]	1.5* ^[m]	1.5 ^[p]
$\partial G/\partial T$ (GPa/K)	-0.013 ^[b]	-0.017 ^[g,i]	-0.016 ^[c,k]	-0.015* ^[m]	-0.01 ^[o]
α^*10^6 (K ⁻¹)	27 ^[f]	20 ^[i]	18.7 ^[l]	17.3 ^[m]	25 ^[n]
b^*10^8 (K ⁻²)	0.9 ^[f]	2.5 ^[i]	0.42 ^[l]	1.6 ^[m]	0.9 ^[n]
	Akimotoite	Stishovite	Magnesiowüstite	Perovskite	
ρ (g/cm ³)	3.81+1.03*XFe+0.784* XA1 ^[ab]	4.29 ^[c]	3.583+ 2.28*XFe ^[c]	4.108+ 1.4*XFe ^[c]	
K _{So} (GPa)	214 ^[s,v]	316 ^[c]	166 ^[w]	253 ^[y]	
K _{So'}	4.2 ^[v]	4 ^[c]	4 ^[u,w]	4.4 ^[y]	
$\partial K_S/\partial T$ (GPa/K)	-0.017 ^[c]	-0.027 ^[c]	-0.016 ^[c]	-0.021 ^[y]	
G ₀ (GPa)	132 ^[c,s,v]	220 ^[c]	112 ^[w]	170 ^[y]	
G _{0'}	1.32 ^[v]	1.8 ^[c]	1.9 ^[w]	2 ^[y]	
$\partial G/\partial T$ (GPa/K)	-0.017 ^[c]	-0.018 ^[c]	-0.024 ^[c]	-0.028 ^[y]	
α^*10^6 (K ⁻¹)	24.1 ^[r]	12.6 ^[t]	38.4 ^[x]	16.4 ^[z]	
b^*10^8 (K ⁻²)	0.3 ^[r]	1.29 ^[t]	0.94 ^[x]	0.86 ^[z]	

*at 6.5 GPa and room temperature.

^a, Isaak, 1992; ^b, Liu et al., 2005b; ^c, Duffy and Anderson, 1989; ^d, Abramson et al., 1997; ^e, Zha et al., 1998; ^f, Guyot et al., 1996; ^g, Li et al., 1998; ^h, Li et al., 1996; ⁱ, Li et al., 2001; ^j, Li, 2003; ^k, Sinogeikin et al., 2003; ^l, Meng et al., 1994; ^m, Kung et al., 2005; ⁿ, Wang et al., 1998; ^o, Sinogeikin and Bass, 2002; ^p, Gwanmesia et al., 2006; ^q, Liu et al., 2000; ^r, Wang et al., 2004; ^s, Weidner and Ito, 1985; ^t, Nishihara et al., 2005; ^u, Li and Liebermann, 2007; ^v, Zhou et al., 2011; ^w, Kung et al., 2002; ^x, Fei et al., 1992; ^y, Li and Zhang, 2005; ^z, Wang et al., 1994; ^{aa}, Woodland and Angel, 1997; ^{ab}, Xu et al., 2008.

relations and mineral variations for harzburgite are based on this study, and those for pyrolite and basalt are from *Irifune and Ringwood* [1987a]. The following Clapeyron slopes of the phase transitions involved were used in this study, olivine-wadsleyite: 0.0036 GPa/K [Morishima et al., 1994], wadsleyite-ringwoodite: 0.00691 GPa/K [Suzuki et al., 2000], ringwoodite-perovskite + magnesiowüstite: -0.0013 GPa/K [Fei et al., 2004], garnet-stishovite+ringwoodite: 0.006 GPa/K [Sawamoto, 1987], stishovite+ringwoodite-akimotoite: -0.002 GPa/K [Sawamoto, 1987], akimotoite-perovskite: -0.0029 GPa/K [Ito and Takahashi, 1989; Ono et al., 2001; Hirose et al., 2001; Fei et al., 2004], clinopyroxene-garnet: 0.002 GPa/K [Irifune and Ringwood, 1987b]. Effects of major element partitioning are taken into account whenever composition dependence on density and elasticity is available.

[17] Density profiles of harzburgite and pyrolite were calculated along a chosen subduction zone geotherm [Litasov et al., 2006] and a “normal” mantle geotherm [Katsura et al., 2010], respectively (Figure 7a). Figure 7b shows the difference in density between the two profiles. Harzburgite is ~0.1 g/cm³ denser than pyrolite between ~420 and 650 km, and ~0.2 g/cm³ less dense between 650 and 680 km. Figure 7c shows vertically integrated

density contrast of a detached harzburgite layer relative to the surrounding mantle as a function of mean layer depth. The buoyancy contrast was obtained by assuming a slab stagnant at different depths, with integrated density contrast over the entire vertical slab thickness. The integrated density contrast, denoted by $D(h)_{\text{integrate}}$, is calculated using

the following equation:
$$D(h)_{\text{integrate}} = \int_{H_{\text{top}}}^{H_{\text{bottom}}} (\rho_{\text{harzburgite}} - \rho_{\text{pyrolite}}) g dH$$
, where h is the average depth of the stagnant slab, H_{top} and H_{bottom} are the depths of the top and bottom surfaces of the slab, respectively, $\rho_{\text{harzburgite}}$ and ρ_{pyrolite} are the density of harzburgite and pyrolite, respectively, and g is gravitational acceleration. Through integration, $D(h)_{\text{integrate}}$ represents density contrast-induced normal stress in the vertical direction, in units of (g/cm³)(N/kg)(km) = (10³kg/m³)(N/kg)(10³m) = 10⁶ Pa = MPa.

[18] For various thicknesses from 20 to 80 km, the harzburgite layer is denser in the MTZ until ~660 km depth owing to combined effects of composition, thermal, and phase relations. Considering the upper basalt layer, however, the overall subducted oceanic lithosphere is denser than the surrounding mantle (Figure 8) and slabs will be driven to the bottom of the MTZ.

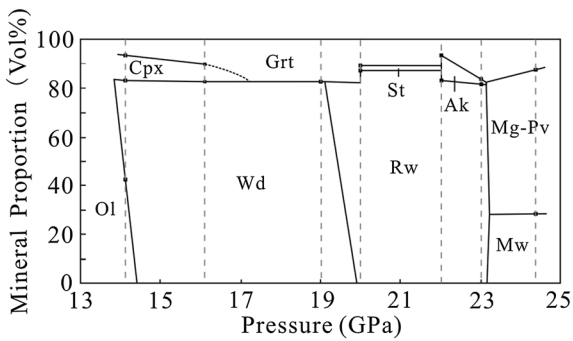


Figure 5. Variation of mineral proportions in harzburgite as a function of pressure at 1673 K. Mineral abbreviations are the same as in Figure 4.

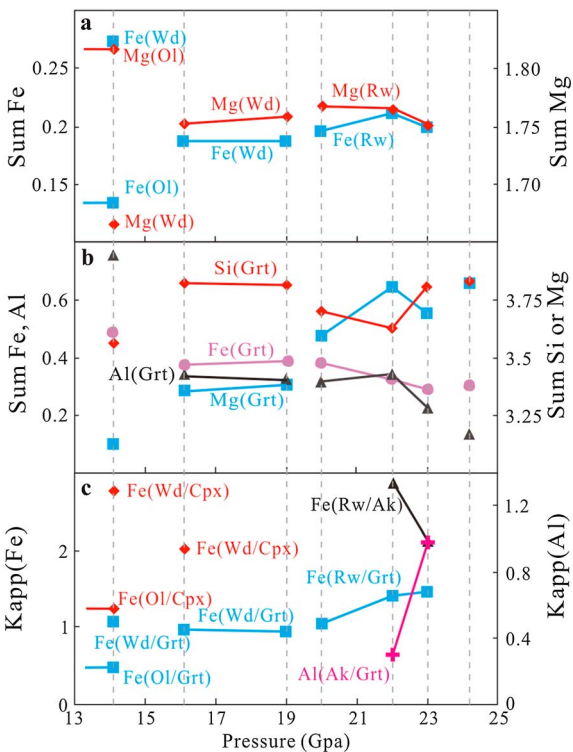


Figure 6. (a) Variations in mineral compositions of the olivine-normative component (number of oxygen = 4) with pressure at 1673 K. (b) Variations in mineral compositions of garnet (number of oxygen = 12) with pressure at 1673 K. Diamonds and squares represent concentrations of Si and Mg, respectively (vertical axis to the right). Triangles and circles represent concentrations of Al and Fe (vertical axis to the left). (c) Variations in partition coefficient of Fe between olivine, wadsleyite, ringwoodite and clinopyroxene, garnet, akimotoite with pressure at 1673 K (vertical axis to the left), as indicated by diamonds, squares, and triangles; vertical axis to the right indicates partition coefficient of Al (magenta crosses) between akimotoite and garnet.

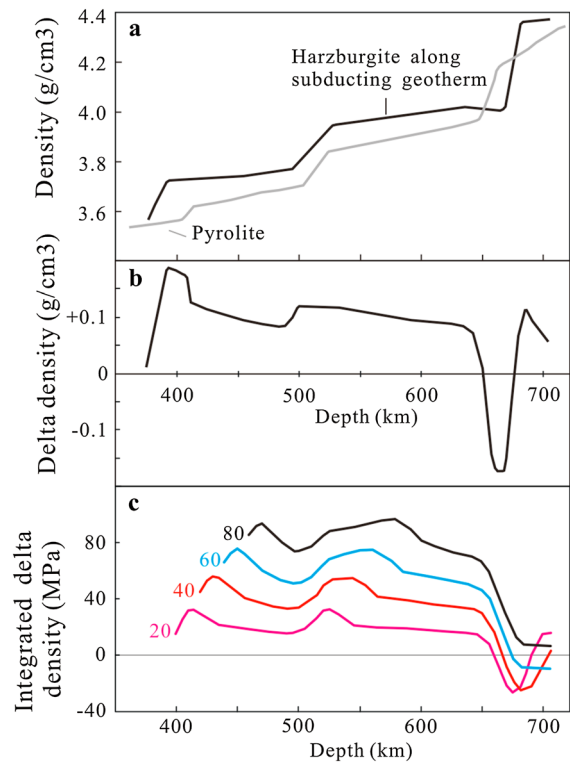


Figure 7. (a) Density profiles of harzburgite (black) and pyrolite (grey) along a typical slab geotherm [Litasov *et al.*, 2006] and a “normal” mantle geotherm [Katsura *et al.*, 2010]. (b) Density of harzburgite relative to that of pyrolite along the same geotherms as in a. (c) Buoyancy of a detached harzburgite layer as represented by vertically integrated density contrast between harzburgite and the ambient mantle (in force per unit area) as a function of layer thickness (in kilometers as indicated next to the curves). Here we assume a harzburgite layer stagnant at different depths and calculate the vertical integrated density contrast from the top of the harzburgite layer to the bottom. Negative values correspond to float direction.

[19] Mantle dynamics is a complex process and cannot be determined by simple gravitation buoyancy alone. Karato [1997] analyzed the mechanical behavior of subducted lithosphere and concluded that if garnets in the crustal component of the slab possess higher strength relative to the surrounding mantle, mechanical interaction may result in “peeling” of the crustal layer from harzburgite by folding. The decoupled harzburgite layer alone will be negatively buoyant and sink toward the bottom of the MTZ. On the other hand, slab bending moment, viscosity variations, and trench rollback dynamics [e.g., Bina and Kawakatsu, 2010] may provide positive buoyancy forces for the subducted slab as a whole. Beneath eastern China, numerous high-resolution seismic

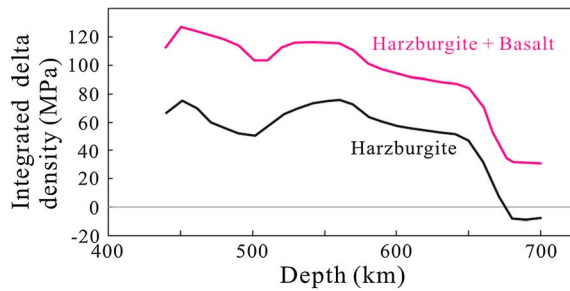


Figure 8. Buoyancy of subducted slab (harzburgite + basalt) as represented by vertically integrated density contrast between the slab and the ambient mantle (in force per unit area) as a function of depth. The thickness of harzburgite is 60 km and basalt is 15 km (buoyancy of the harzburgite layer alone is also shown for comparison). Negative values correspond to float direction.

studies have shown that high P-wave velocity anomalies are located inside the MTZ; no clear fast anomalies exist below the 660 km discontinuity [e.g., *Huang and Zhao, 2006; Zhao et al., 2009; Li and van der Hilst, 2010; Pei and Chen, 2010*]. In the following, we attempt to model the thermal and physical properties of the anomalies beneath eastern China, by assuming that they are due to subducted oceanic lithosphere in the MTZ.

4.2. Thermal Modeling of the Subducting Slab for Eastern China: Two End-Member Models

[20] Two slab models were considered in this study. We examine a horizontal length of stagnated slab of ~1500 km (white boxes in Figure 9), corresponding to recent tomography studies beneath eastern China [e.g., *Huang and Zhao, 2006; Li and van der Hilst, 2010*]. Slab thermal models were calculated using the kinematic finite-difference heat-transfer algorithm TEMSPOL [*Negredo et al., 2004*], as modified by *Bina and Kawakatsu [2010]* to allow prescribed changes in slab dip angle at depth, with further modification to allow for deformation of the stagnant slab in the MTZ. Thermal structure was calculated assuming uniform thermal conductivity throughout the region of interest; lateral temperature variations arise largely from the residence time of the stagnant slab.

[21] Model I deals with a standard flat slab, in which a slab subducts into the MTZ and bends to become horizontal just above the 660 km seismic discontinuity, similar to that modeled in *Bina and Kawakatsu [2010]*. We adopted the following thermal parameters appropriate for Japan Wadati-Benioff zone and east China: a 130 Ma lithosphere with a convergence rate of 8.5 cm/yr and a dip angle of 35°. We assumed a slab thickness of

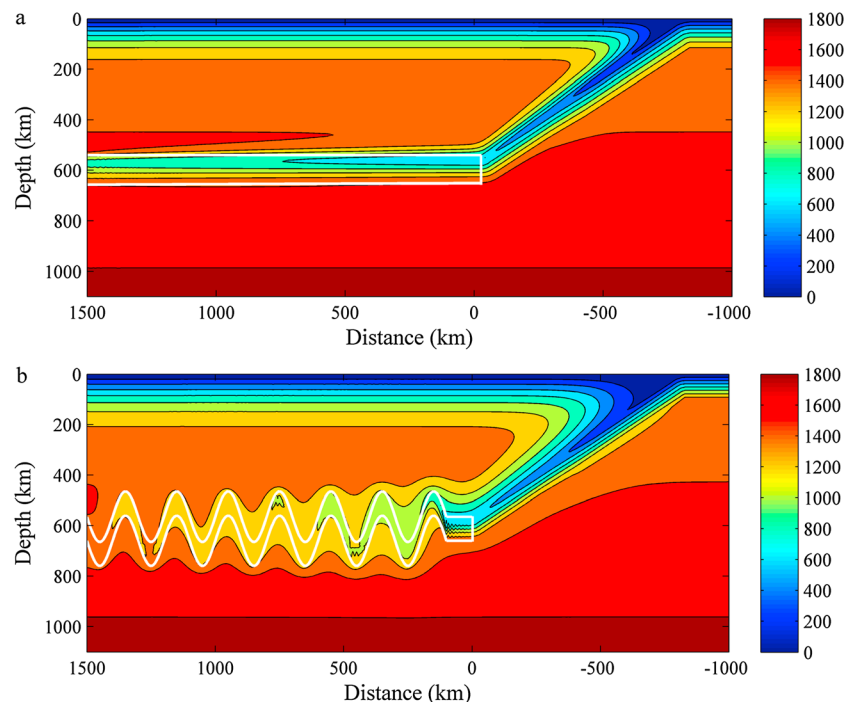


Figure 9. Details of the thermal structure in slab models I and II. White lines demark the stagnant slab. (a) Thermal structure of model I. (b) Thermal structure of model II. Temperature contours and color bars are labeled in Celsius.

120 km, consisting of a top basalt upper layer of 15 km, a harzburgite layer of 60 km, and a lherzolite layer of 45 km, to approximate thickening by pure-shear deformation of the slab within the MTZ, with a uniform thermal conductivity of 3.2 W/m/K throughout. Detailed temperature distribution in the slab is given in Figure 9a.

[22] Model II kinematically takes into account an undulated (buckled) slab, a geometry that is increasingly recognized as a consequence of trench retreat and rheological contrast with the surrounding mantle (e.g., Christensen, 2001; Schmid *et al.*, 2002; Ribe *et al.*, 2007; Yoshioka and Naganoda, 2010; Lee and King, 2011; Li and Ribe, 2012; Čížková and Bina, 2012). Buckling deformation of the stagnant slab is represented by imposing, after the first 100 km of horizontal offset, a sinusoidal oscillation with both horizontal half-wavelength and vertical amplitude of 100 km. (Note that $\lambda=200$ km is chosen as a contrasting end member to the effective $\lambda=\infty$ of the flat slab; oscillation periods in recent dynamic models [Lee and King, 2011; Čížková and Bina, 2012] suggest that $\lambda=1000$ km may be a more physically realistic intermediate value, although real slabs are unlikely to exhibit strictly harmonic buckling.) This model has an upper harzburgite layer of 45 km underlain by a depleted peridotite (lherzolite) layer of 50 km; the lherzolite layer in both models is approximated by pyrolite. The upper basalt layer is assumed to be separated from the subducted lithosphere due to folding of the slab and viscosity contrast between the crustal layer and surrounding mantle [Karato, 1997]. Figure 9b shows the thermal structure of the undulated slab model. Basic slab parameters were identical to the straight slab model (dip = 35°, velocity = 8.5 cm/yr, age = 130 Ma), except for a thermal conductivity of 4 W/m/K.

[23] The calculated temperatures in the straight slab range from 1100 to 1873 K throughout the slab, greater than the thermal variations estimated by joint mineral physics and seismic travel-time analysis (1400–1600 K) [Ritsema *et al.*, 2009], but with a similar mean value. The buckled slab has relatively high temperatures, ca. 1273–1673 K, similar to those obtained by Ritsema *et al.* [2009], as a result of the greater slab residence time and thermal equilibration within the MTZ in model II.

4.3. Velocity Signatures of the Slab Models

[24] The widely used Voigt-Reuss-Hill averaging method was adopted to approximate the aggregate velocities, assuming that harzburgite, pyrolite, and basalt are all isotropic mineral aggregates [Watt

et al., 1976; Bina and Helffrich, 1992]. Thermoeastic parameters of major minerals listed in Table 4 and variations of mineral proportions based on this study and Irifune and Ringwood [1987a] are used to calculate velocities of harzburgite, pyrolite, and basalt at HPHT conditions. Because of compositional similarity between lherzolite and the surrounding mantle (e.g., pyrolite), the lherzolite layer in both models is approximated by pyrolite; all layers are assumed dry. Major phases in the two models are shown in Figures 10a and 11a, respectively. In the straight slab model, the harzburgite layer is mainly composed of ringwoodite, garnet, and stishovite. In the undulated slab model, ringwoodite, garnet, akimotoite, and stishovite are the main constituent minerals.

[25] Figure 10b–d shows velocity and density signatures in model I. The velocity and density anomalies are calculated relative to a pyrolitic mantle and are given in percent. P- and S-wave velocities of the basalt layer are about 2–3% slower than the surrounding mantle, consistent with recent ultrasonic measurements on oceanic crustal materials [Kono *et al.*, 2007] and seismically observed anomalies under southern Africa [Shen and Blum, 2003], where a layer of accumulated oceanic crust was proposed to be stagnant. The harzburgite layer exhibits high velocities between ~550 and 620 km depths (Figure 10b and c) due to lower slab temperature and higher ringwoodite content than the surrounding mantle (Figure 5). Relative to the surrounding mantle, anomalies are +3–5% and +4.5–7.5%, respectively, for Vp and Vs. Figure 10d shows density anomalies caused by the stagnant slab. The upper basalt layer is about 5–8% denser than the surrounding pyrolitic mantle due to its high garnet content. The middle harzburgite layer and the lower depleted pyrolite layer are about 1–3% and 0–1% denser than pyrolitic mantle, respectively, due to the relatively low temperature in these layers.

[26] Figure 11b–d shows the velocity and density signatures in model II. Amplitudes of the calculated anomalies relative to a pyrolitic mantle are ~2–3.5% and 3–5% for Vp and Vs, respectively (Figure 11b and d). The relative low magnitudes of velocity anomalies in model II are primarily due to higher temperatures. Density anomalies (relative to pyrolite mantle) are about 4–6% in the upper part of MTZ, mainly caused by the relatively higher wadsleyite content in the harzburgite layer relative to pyrolite (Figure 11d). In the lower part of MTZ, density anomalies are about 0–2%, caused by relatively low temperature and high ringwoodite content.

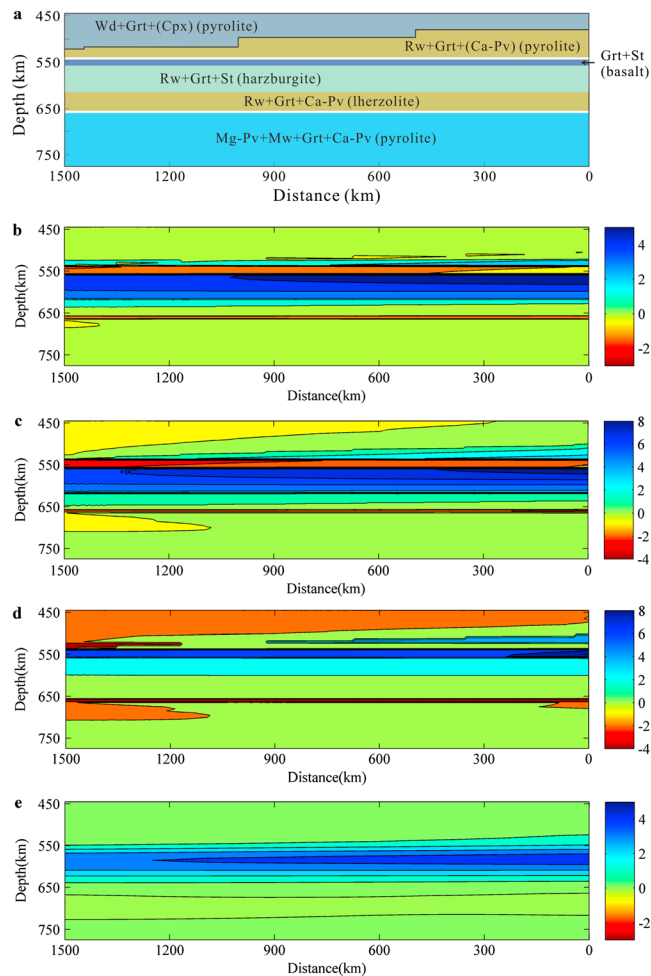


Figure 10. A segment of the horizontal slab in model I. (a) Minerals and their distribution in the slab; the mineral assemblage of harzburgite is based on our experimental results, and for those of basalt and pyrolite, see *Irifune and Ringwood* [1987a]. (b–d) V_p , V_s , and density anomalies (in percent) caused by the stagnant slab relative to a pyrolite mantle. (e) P-wave velocity anomalies after applying low-pass Gaussian spatial filters.

5. Discussion: Stagnant Slab under Eastern China—Straight or Buckled?

5.1. Comparison with Seismic Tomography Data

[27] Before comparing mineral physics results with seismic tomography studies, effects of quality factor Q on seismic velocities need to be considered [e.g., *Karato*, 1993]. Anharmonicity contributions to temperature dependence of seismic velocities become especially important when Q is low. However, an accurate estimate of the effect of Q on seismic velocities is difficult because anelasticity of high-pressure minerals is poorly known. For a first-order approximation, we assume Q values for the slab and the surrounding mantle to be of the same magnitude (~ 400 , see *Dziewonski and Anderson*, 1981). We then estimate the resultant $-\Delta V_p/V_p$

caused by anelasticity using the $\partial \ln V_p / \partial T$ profile presented by *Karato* [1993], assuming that average temperatures are approximately 1273 and 1773 K for the stagnant slab and the surrounding mantle, respectively. The corresponding $-\Delta V_p/V_p$ values are very similar, about 0.01–0.02 and 0.01–0.03 for the stagnant slab and the surrounding mantle, respectively. Therefore, the effect of anelasticity is (to first order) to decrease the overall velocities by ~ 1 –2%, without affecting velocity anomalies (i.e., relative velocity contrast) in our calculation results.

[28] Seismic tomography studies, relying primarily on P-wave travel times, report maximum P-wave velocity anomalies about +1–2% relative to average seismological mantle models (e.g., *iasp91*, *Kennett and Engdahl*, 1991) beneath eastern China [e.g., *Huang and Zhao*, 2006; *Li and van der Hilst*, 2010; *Pei and Chen*, 2010], much lower than that

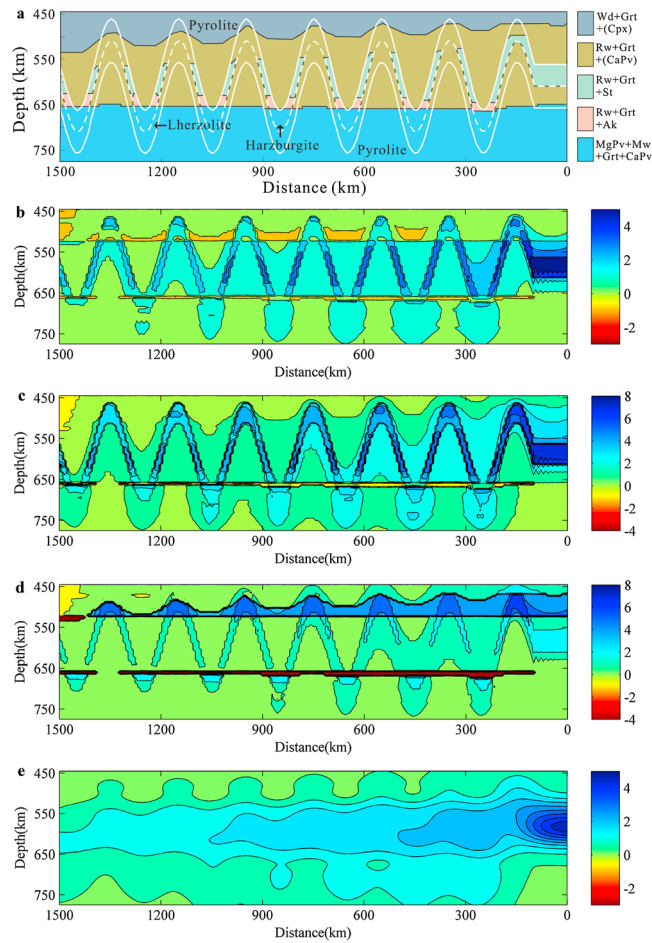


Figure 11. A segment of the undulated slab in model II. (a) Minerals and their distribution in the slab. (b–d) V_p , V_s , and density anomalies (in percent) caused by the stagnant slab relative to a pyrolite mantle. (e) P-wave velocity anomalies after applying low-pass Gaussian spatial filters.

obtained by our mineral physics models. At least two important factors must be considered when comparing mineralogically derived velocity images with those obtained by seismic tomography studies. First, tomographic images generally underestimate magnitudes of velocity anomalies, because “regularization” of the tomographic inversion reduces the amplitudes of anomalies. Second, tomographic images are generally “smeared” both laterally and vertically (i.e., they are effectively low-pass filtered), so that sharp (i.e., high-frequency) features are damped, thereby spreading anomalies spatially while reducing their local magnitudes. Although we cannot fully reproduce the former in our mineralogical images, we attempt to approximate the latter by applying low-pass spatial (essentially moving-window) filtering to the mineralogical images. (In doing so, we assume spatially uniform tomographic resolution, as modeling the actual spatially varying resolution would require

greater knowledge of details of the seismological data set used to constrain the velocity inversion).

[29] Here we assumed that the horizontal and vertical resolutions under eastern China are about 300 km and 100 km, respectively, roughly consistent with recent tomography studies [e.g., *Li and van der Hilst, 2010*]. We then convolved horizontal (6σ in 300 km) and vertical (6σ in 100 km) Gaussian filters with the mineralogical P-wave velocity structure, as most tomography studies were based on V_p . Figures 10e and 11e show results after convolving a 300×100 km Gaussian filter with two model structures of the MTZ (Figures 10b and 11b). For model I, the low-velocity region caused by the upper basalt layer disappear due to the reduction in spatial resolution. Amplitudes of the P-wave anomalies caused by the harzburgite layer are reduced by a factor of ~ 2 for the horizontal slab model to about 1.5–3.5%, still significantly higher than seismic tomography results.

In addition, the fast anomalies persist to much greater distance than seismic tomography detects. For model II, the sharp, sinusoidal velocity anomalies are smeared to a smooth near-horizontal feature. The amplitude of P-wave velocity anomalies is reduced to about 1–2% throughout the slab except for where slab just enters the MTZ (Figure 11e). The horizontal extent of the fast anomaly is greatly reduced compared to model I. Overall, the buckled model (after filtering) better matches the P-wave anomalies observed in seismic tomography.

5.2. Comparison with Seismic TriPLICATION Models

[30] Analyses of P- and S-wave triplication near the 660 km discontinuity provide more details on velocity variations with depth at the bottom of MTZ. Unfortunately, it is difficult to derive quantitative error bounds on discontinuity depths and amplitudes from triplication data [Kennett and Engdahl, 1991], due in part to the inherent trade-offs between the discontinuity properties

(sharpness, topography, etc.) and velocities immediately below and above the discontinuities. An advantage of this type of modeling, however, is that it often provides a complete velocity versus depth profile extending from the MTZ to the top of lower mantle.

[31] For model I, the (unfiltered) P-wave velocity anomaly amplitudes (3–5%) are significantly greater than those in the triplication studies for east China (Figure 12). These velocity profiles of mineral physics models have been corrected for anelasticity effects as we discussed earlier. On the other hand, simulating numerically effects of slab buckling on seismic triplication based on model II is beyond the scope of this study. A main effect of lateral variation in seismic structure would be to introduce greater uncertainties into the depths of seismic velocity contrasts and their adjacent velocity gradients, thereby reducing the apparent anomaly magnitudes. Despite the uncertainties in velocity magnitude comparison, it is informative to examine the nature of velocity variation with depth. All P-wave triplication models for eastern China exhibit anomalously high gradients

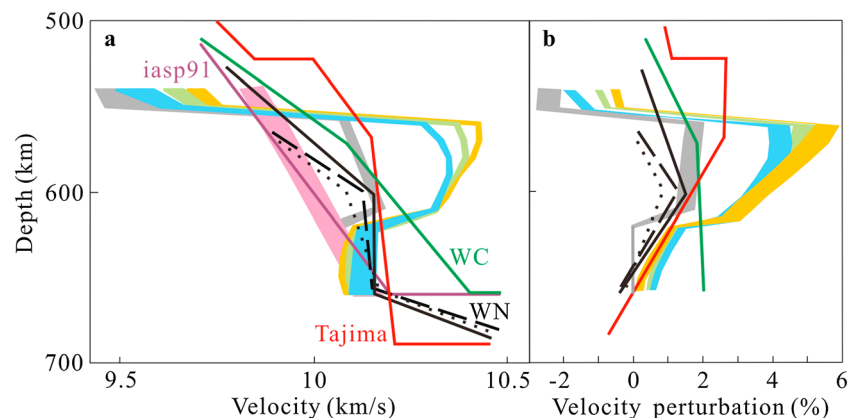


Figure 12. Seismic triplication profiles compared with our mineral physics slab models. (a) P-wave velocity profiles as a function of depth from our slab model I and triplication studies. Purple line represents the global average seismic model iasp91. Magenta-shaded zone is calculated pyrolite velocity. Model slab velocity profiles are plotted as orange, green, and blue curves at distances 0, 750, and 1500 km, respectively; the corresponding minimum slab temperatures at these locations are 1273, 1073, and 873 K, respectively. Grey-shaded curve represents slab velocities at thermal equilibrium with the surrounding mantle. The widths of all model velocity curves (including that of pyrolite) represent uncertainties in the present calculation: lower velocity limits are based on the elastic parameters of garnet from *Irifune et al.* [2008] and upper limits are based on the elastic parameters of garnet listed in Table 4. Curves labeled with “Tajima”, “WC”, and “WN” are velocity profiles from triplication studies [Tajima et al., 2009; Wang and Chen, 2009; Wang and Niu, 2010], respectively. Black dotted, dash, and solid lines labeled with “WN” are the fast anomalies observed progressively farther away from the Wadati-Benioff zone beneath Kurile-Honshu. (b) P-wave velocity perturbation profiles correspond to those in a. Velocity anomalies in our model are calculated relative to a pyrolite mantle “baseline”, while seismic anomalies are estimated by subtracting the standard mantle velocity model (iasp91, Kennett and Engdahl, 1991) from local triplication models. Widths of the lines represent calculated uncertainties. Uncertainties for the depleted pyrolite layer (below ~630 km depth) are significantly less, as the mineralogy is assumed identical to pyrolite in our model.

above ~600 km and much lower, or even negative, gradients below (Figure 12); both of these features are observed in our kinematic models. Of course, the undulating shape of the slab simulated here is schematic and highly simplified. For seismic signals dominated by wavelengths comparable to or shorter than slab undulation wavelengths, seismic waveforms will be most distorted. The lack of direct knowledge of the shape of the slab in this region makes direct comparison with triplication data impossible. However, recent analysis [Stähler *et al.*, 2012] incorporating finite-frequency effects, by which “rays” sample a broader region of the MTZ, suggests that triplication signatures can still be recovered in the presence of meaningful topography.

[32] Buckling of subducted oceanic lithosphere has been observed in both numerical studies with complex geometries and rheologies and in laboratory simulation experiments [e.g., Christensen, 2001; Schmid *et al.*, 2002; Bellahsen *et al.*, 2005; Ribe *et al.*, 2007]. Numerical models have shown that slab thickening observed in seismic tomographic images cannot be explained by “pure shear” deformation, which can only thicken the slab by at most a factor of two, but can be easily interpreted by the buckling mechanism [Ribe *et al.*, 2007]. Recent numerical results also show that slab buckling may be a universal feature in many subduction zones, and can reconcile a variety of puzzling geological and geophysical observations, especially when the slab has a relatively slow trench migration and a relatively large viscosity increase across the 660 km discontinuity [Lee and King, 2011; Čížková and Bina, 2012]. In the present study, we provide additional evidence for the slab buckling model through kinematic thermal structure analysis and mineral physics calculations. Although only two end-member models are analyzed, the consistency of velocity signatures between our buckled slab model and seismic observations indicates that a certain degree of buckling should represent the real behavior of the stagnated slabs beneath eastern China.

6. Conclusions

[33] We present HPHT experimental results on a natural harzburgite under MTZ conditions and provide important constraints on the mineralogical constituents of subducted harzburgite materials. The buoyancy relationships between subducting oceanic lithosphere and surrounding mantle provide supporting evidence for the stagnation of subducted slabs. Velocity and density signatures

of stagnated slabs were calculated based on two end-member slab geometries and composition, based on kinematic thermal structure analysis. These are forward model predictions, not fits to seismic observations. Examination of these predictions in light of seismic analysis suggests several important conclusions. (1) The fast anomalies and velocity structures observed under eastern China can be explained by subducted materials stagnant in the MTZ. (2) The harzburgite layer, subjected to some degree of undulation (buckling), is primarily responsible for the fast anomalies, whose magnitudes are in good accordance with seismic tomography studies. (3) The absence of an apparent low-velocity basalt layer in seismic models suggests that the basalt layer is either very thin (therefore nonresolvable seismically) or has been delaminated during subduction. (4) Mineral physics experiments are now capable of providing phase relations and thermoelastic databases for quantitative modeling of the subducted lithosphere. With further improvement in our understanding of slab thermal structure and mechanical coupling with the surrounding mantle, important constraints on the thermal structure, mineralogy, composition, density, and velocities of slab materials in MTZ may be obtained.

Acknowledgments

[34] We thank Chao Wang for useful discussions, Prof. Jianhua Rao for technical developments during the experiments, Prof. Jishun Yu and Dr. Jinhua Zhang for XRD analysis, associate Prof. Tao Chen and Dr. Yungui Liu for micro-Raman analysis, associate Prof. Haijun Xu and Dr. Siyu Feng for FE-SEM analysis, and Dr. Feng Shi for FT-IR analysis. We are grateful to two anonymous reviewers for their critical and constructive comments. This work was supported by the National Natural Science Foundation of China (41174076) and Sinoprobe-0801, and partially by the US NSF (EAR-0968456).

References

- Abramson, E. H., J. M. Brown, L. J. Slutsky, and J. Zaug (1997), The elastic constants of San Carlos olivine to 17 GPa, *J. Geophys. Res.*, *102*, 12253–12263, doi:10.1029/97jb00682.
- Ai, Y., T. Zheng, W. Xu, Y. He, and D. Dong (2003), A complex 660 km discontinuity beneath northeast China, *Earth Planet. Sci. Lett.*, *212*, 63–71, doi:10.1016/S0012-821X(03)00266-8.
- Bell, D. R., P. D. Ihinger, and G. R. Rossman (1995), Quantitative analysis of trace OH in garnet and pyroxenes. *Am. Mineral.*, *80*, 465–474.
- Bell, D. R., G. R. Rossman, J. Maldener, D. Endisch, and F. Rauch (2003), Hydroxide in olivine: A quantitative determination of the absolute amount and calibration of the IR spectrum. *J. Geophys. Res.*, *108*, 2105, doi:10.1029/2001JB000679.

- Bellahsen, N., C. Faccenna, and F. Funiciello (2005), Dynamics of subduction and plate motion in laboratory experiments: Insights into the "plate tectonics" behavior of the Earth, *J. Geophys. Res.*, *110*, B01401, doi:10.1029/2004jb002999.
- Bina, C. R., and G. R. Helffrich (1992), Calculation of elastic properties from thermodynamic equation of state principles, *Annu. Rev. Earth Planet. Sci.*, *20*, 527-552, doi:10.1146/annurev.ea.20.050192.002523.
- Bina, C. R., and H. Kawakatsu (2010), Buoyancy, bending, and seismic visibility in deep slab stagnation, *Phys. Earth Planet. Inter.*, *183*, 330-340, doi:10.1016/j.pepi.2010.04.010.
- Chen, L., and Y. Ai (2009), Discontinuity structure of the mantle transition zone beneath the North China Craton from receiver function migration, *J. Geophys. Res.*, *114*, B06307, doi:10.1029/2008jb006221.
- Christensen, U. (2001), Geodynamic models of deep subduction, *Phys. Earth Planet. Inter.*, *127*, 25-34, doi:10.1016/S0031-9201(01)00219-9.
- Čížková, H., and C. R. Bina (2012), Time-varying subduction and rollback velocities in slab stagnation and buckling, *Eos Trans. AGU*, *93*, Fall Meet. Suppl., abst. D111A-2394.
- Dick, H. J. B., and J. H. Natland (1996), Late-state melting evolution and transport in the shallow mantle beneath the East Pacific Rise, in Proceedings of the Ocean Drilling Program, Scientific Results, vol. 147, edited by C. Mével, K. M. Gölüs, J. F. Allan and P. S. Meyer, pp.103-134, Ocean Drilling Program, College Station, TX.
- Duffy, T. S., and D. L. Anderson (1989), Seismic velocities in mantle minerals and the mineralogy of the upper mantle, *J. Geophys. Res.*, *94*, 1895-1912, doi:10.1029/JB094iB02p01895.
- Dziewonski, A. M., and D. L. Anderson (1981), Preliminary reference Earth model, *Phys. Earth Planet. Inter.*, *25*, 297-356, doi:10.1016/0031-9201(81)90046-7.
- Fabrichnaya, O. B. (1995), Thermodynamic data for phases in the FeO-MgO-SiO₂ system and phase relations in the mantle transition zone, *Phys. Chem. Miner.*, *22*, 323-332, doi:10.1007/bf00202773.
- Fei, Y., and C. M. Bertka (1999), Phase transitions in the Earth's mantle and mantle mineralogy, in *Mantle Petrology: Field Observations and High Pressure Experimentation*, edited by Y. Fei and C. M. Bertka, pp. 189-207, The Geochemical Society, Houston.
- Fei, Y., H. K. Mao, J. Shu, and J. Hu (1992), P-V-T equation of state of magnesiowüstite (Mg_{0.6}Fe_{0.4})O, *Phys. Chem. Miner.*, *18*, 416-422, doi:10.1007/bf00200964.
- Fei, Y., et al. (2004), Experimentally determined postspinel transformation boundary in Mg₂SiO₄ using MgO as an internal pressure standard and its geophysical implications, *J. Geophys. Res.*, *109*, B02305, doi:10.1029/2003jb002562.
- Fukao, Y., M. Obayashi, H. Inoue, and M. Nishii (1992), Subducting slabs stagnant in the mantle transition zone, *J. Geophys. Res.*, *97*, 4809-4822, doi:10.1029/91jb02749.
- Fukao, Y., M. Obayashi, T. Nakakuki, and T. D. S. P. Group (2009), Stagnant slab: A review, *Annu. Rev. Earth Planet. Sci.*, *37*, 19-46, doi:10.1146/annurev.earth.36.031207.124224.
- Fukao, Y., S. Widiyantoro, and M. Obayashi (2001), Stagnant slabs in the upper and lower mantle transition region, *Rev. Geophys.*, *39*, 291-323, doi:10.1029/1999rg000068.
- Guyot, F., Y. Wang, P. Gillet, and Y. Ricard (1996), Quasi-harmonic computations of thermodynamic parameters of olivines at high-pressure and high-temperature: A comparison with experiment data, *Phys. Earth Planet. Inter.*, *98*, 17-29, doi:10.1016/S0031-9201(96)03174-3.
- Gwanmesia, G. D., J. Zhang, K. Darling, J. Kung, B. Li, L. Wang, D. Neuville, and R. C. Liebermann (2006), Elasticity of polycrystalline pyrope (Mg₃Al₂Si₃O₁₂) to 9 GPa and 1000°C, *Phys. Earth Planet. Inter.*, *155*, 179-190, doi:10.1016/j.pepi.2005.10.008.
- Hirose, K., Y. Fei, Y. Ma, and H. K. Mao (1999), The fate of subducted basaltic crust in the Earth's lower mantle, *Nature*, *397*, 53-56, doi:10.1038/16225.
- Hirose, K., T. Komabayashi, M. Murakami, and K. Funakoshi (2001), In situ measurements of the majorite-akimotoite-perovskite phase transition boundaries in MgSiO₃, *Geophys. Res. Lett.*, *28*, 4351-4354, doi:10.1029/2001gl013549.
- Huang, J., and D. Zhao (2006), High-resolution mantle tomography of China and surrounding regions, *J. Geophys. Res.*, *111*, B09305, doi:10.1029/2005jb004066.
- Irfune, T., and M. Isshiki (1998), Iron partitioning in a pyrolyte mantle and the nature of the 410-km seismic discontinuity, *Nature*, *392*, 702-705, doi:10.1038/33663.
- Irfune, T., and A. E. Ringwood (1987a), Phase transformations in primitive MORB and pyrolyte compositions to 25 GPa and some geophysical implications, in *High-Pressure Research in Mineral Physics: A Volume in Honor of Syun-iti Akimoto*, Geophys. Monogr. Ser., vol. 39, edited by M. H. Manghnani and Y. Syono, pp. 231-242, AGU, Washington, D. C.
- Irfune, T., and A. E. Ringwood (1987b), Phase transformations in a harzburgite composition to 26 GPa: Implications for dynamical behaviour of the subducting slab, *Earth Planet. Sci. Lett.*, *86*, 365-376, doi:10.1016/0012-821X(87)90233-0.
- Irfune, T., and A. E. Ringwood (1993), Phase transformations in subducted oceanic crust and buoyancy relationships at depths of 600-800 km in the mantle, *Earth Planet. Sci. Lett.*, *117*, 101-110, doi:10.1016/0012-821X(93)90120-X.
- Irfune, T., Y. Higo, T. Inoue, Y. Kono, H. Ohfuji, and K. Funakoshi (2008), Sound velocities of majorite garnet and the composition of the mantle transition region, *Nature*, *451*, 814-817, doi:10.1038/nature06551.
- Isaak, D. G. (1992), High-temperature elasticity of iron-bearing olivines, *J. Geophys. Res.*, *97*, 1871-1885, doi:10.1029/91jb02675.
- Ito, E., and H. Yamada (1982), Stability relations of silicate spinels, ilmenites, and perovskites, in *High-Pressure Research in Geophysics, Advances in Earth and Planetary Sciences*, edited by S. Akimoto and M. H. Manghnani, pp.405-419, Center for Academic Publication, Japan.
- Ito, E., and E. Takahashi (1989), Postspinel transformations in the system Mg₂SiO₄-Fe₂SiO₄ and some geophysical implications, *J. Geophys. Res.*, *94*, 10637-10646, doi:10.1029/JB094iB08p10637.
- Karato, S. (1993), Importance of anelasticity in the interpretation of seismic tomography, *Geophys. Res. Lett.*, *20*, 1623-1626, doi:10.1029/93GL01767.
- Karato, S. (1997), On the separation of crustal component from subducted oceanic lithosphere near the 660 km discontinuity, *Phys. Earth Planet. Inter.*, *99*, 103-111, doi:10.1016/S0031-9201(96)03198-6.
- Katsura, T., A. Yoneda, D. Yamazaki, T. Yoshino, and E. Ito (2010), Adiabatic temperature profile in the mantle, *Phys. Earth Planet. Inter.*, *183*, 212-218, doi:10.1016/j.pepi.2010.07.001.
- Katsura, T., and E. Ito (1989), The system Mg₂SiO₄-Fe₂SiO₄ at high pressures and temperatures: Precise determination of stabilities of olivine, modified spinel, and spinel, *J. Geophys. Res.*, *94*, 15663-15670, doi:10.1029/JB094iB11p15663.
- Katsura, T., et al. (2004), Olivine-wadsleyite transition in the system (Mg,Fe)₂SiO₄, *J. Geophys. Res.*, *109*, B02209, doi:10.1029/2003jb002438.
- Kennett, B. L. N., and E. R. Engdahl (1991), Travel times for global earthquake location and phase identification, *Geophys. J. Int.*, *105*, 429-465, doi:10.1111/j.1365-246X.1991.tb06724.X.

- Kono, Y., Y. Higo, H. Ohfuji, T. Inoue, and T. Irifune (2007), Elastic wave velocities of garnetite with a MORB composition up to 14 GPa, *Geophys. Res. Lett.*, *34*, L14308, doi:10.1029/2007gl030312.
- Kung, J., B. Li, T. Uchida, and Y. Wang (2005), In-situ elasticity measurement for the unquenchable high-pressure clinopyroxene phase: Implication for the upper mantle, *Geophys. Res. Lett.*, *32*, L01307, doi:10.1029/2004gl021661.
- Kung, J., B. Li, D. J. Weidner, J. Zhang, and R. C. Liebermann (2002), Elasticity of (Mg_{0.83},Fe_{0.17})O ferropericlase at high pressure: Ultrasonic measurements in conjunction with X-radiation techniques, *Earth Planet. Sci. Lett.*, *203*, 557-566, doi:10.1016/S0012-821X(02)00838-5.
- Lee, C., and S. D. King (2011), Dynamic buckling of subducting slabs reconciles geological and geophysical observations, *Earth Planet. Sci. Lett.*, *312*, 360-370, doi:10.1016/j.epsl.2011.10.033.
- Leinenweber, K. D., J. A. Tyburczy, T. G. Sharp, E. Soignard, T. Diedrich, W. B. Petuskey, Y. Wang, and J. L. Mosenfelder (2012), Cell assemblies for reproducible multi-anvil experiments (the COMPRES assemblies), *Am. Mineral.*, *97*, 353-368, doi:10.2138/am.2012.3844.
- Li, B. (2003), Compressional and shear wave velocities of ringwoodite γ -Mg₂SiO₄ to 12 GPa, *Am. Mineral.*, *88*, 1312-1317.
- Li, B., G. D. Gwanmesia, and R. C. Liebermann (1996), Sound velocities of olivine and beta polymorphs of Mg₂SiO₄ at Earth's transition zone pressures, *Geophys. Res. Lett.*, *23*, 2259-2262, doi:10.1029/96gl02084.
- Li, B., and R. C. Liebermann (2007), Indoor seismology by probing the Earth's interior by using sound velocity measurements at high pressures and temperatures, *P. Natl. Acad. Sci.*, *104*, 9145-9150, doi:10.1073/pnas.0608609104.
- Li, B., R. C. Liebermann, and D. J. Weidner (1998), Elastic moduli of wadsleyite (β -Mg₂SiO₄) to 7 gigapascals and 873 kelvin, *Science*, *281*, 675-677, doi:10.1126/science.281.5377.675.
- Li, B., R. C. Liebermann, and D. J. Weidner (2001), P-V-V_p-V_s-T measurements on wadsleyite to 7 GPa and 873 K: Implications for the 410-km seismic discontinuity, *J. Geophys. Res.*, *106*, 30579-30591, doi:10.1029/2001jb000317.
- Li, B., and J. Zhang (2005), Pressure and temperature dependence of elastic wave velocity of MgSiO₃ perovskite and the composition of the lower mantle, *Phys. Earth Planet. Inter.*, *151*, 143-154, doi:10.1016/j.pepi.2005.02.004.
- Li, C., and R. D. van der Hilst (2010), Structure of the upper mantle and transition zone beneath Southeast Asia from traveltimes tomography, *J. Geophys. Res.*, *115*, B07308, doi:10.1029/2009jb006882.
- Li, Z. H., and N. M. Ribe (2012), Dynamics of free subduction from 3-D boundary element modeling, *J. Geophys. Res.*, *117*, B06408, doi:10.1029/2012jb009165.
- Litasov, K. D., E. Ohtani, and A. Sano (2006), Influence of water on major phase transitions in the Earth's mantle, in *Earth's Deep Water Cycle*, Geophys. Monogr. Ser., vol. 168, edited by S. D. Jacobsen and S. van der Lee, pp. 95-111, AGU, Washington, D. C.
- Liu, J., G. Chen, G. D. Gwanmesia, and R. C. Liebermann (2000), Elastic wave velocities of pyrope-majorite garnets (Py₆₂Mj₃₈ and Py₅₀Mj₅₀) to 9 GPa, *Phys. Earth Planet. Inter.*, *120*, 153-163, doi:10.1016/S0031-9201(00)00152-7.
- Liu, Y., S. Gao, C.-T. A. Lee, S. Hu, X. Liu, and H. Yuan (2005a), Melt-peridotite interactions: Links between garnet pyroxenite and high-Mg# signature of continental crust, *Earth Planet. Sci. Lett.*, *234*, 39-57, doi:10.1016/j.epsl.2005.02.034.
- Liu, W., J. Kung, and B. Li (2005b), Elasticity of San Carlos olivine to 8 GPa and 1073 K, *Geophys. Res. Lett.*, *32*, L16301, doi:10.1029/2005gl023453.
- McDonough, W. F., and S. S. Sun (1995), The composition of the Earth, *Chem. Geol.*, *120*, 223-253, doi:10.1016/0009-2541(94)00140-4.
- Meng, Y., Y. Fei, D. J. Weidner, G. D. Gwanmesia, and J. Hu (1994), Hydrostatic compression of γ -Mg₂SiO₄ to mantle pressures and 700 K. Thermal equation of state and related thermoelastic properties, *Phys. Chem. Miner.*, *21*, 407-412, doi:10.1007/bf00203299.
- Michael, P. J., and E. Bonatti (1985), Peridotite composition from the North Atlantic: regional and tectonic variations and implications for partial melting, *Earth Planet. Sci. Lett.*, *73*, 91-104, doi:10.1016/0012-821X(85)90037-8.
- Morishima, H., T. Kato, M. Suto, E. Ohtnai, S. Urakawa, S. Utsumi, O. Shimomura, and T. Kikegawa (1994), The phase boundary between α - and β -Mg₂SiO₄ determined by in situ X-ray observation, *Science*, *265*, 1202-1203, doi:10.1126/science.265.5176.1202.
- Negredo, A. M., J. L. Valera, and E. Carminati (2004), TEMSPOL: A MATLAB thermal model for deep subduction zones including major phase transformations, *Comput. Geosci.*, *30*, 249-258, doi:10.1016/j.cageo.2004.01.002.
- Nishihara, Y., K. Nakayama, E. Takahashi, T. Iguchi, and K. I. Funakoshi (2005), P-V-T equation of state of stishovite to the mantle transition zone conditions, *Phys. Chem. Miner.*, *31*, 660-670, doi:10.1007/s00269-004-0426-7.
- Ono, S., T. Katsura, E. Ito, M. Kanzaki, A. Yoneda, M. J. Walter, S. Urakawa, W. Utsumi, and K. Funakoshi (2001), In situ Observation of ilmenite-perovskite phase transition in MgSiO₃ using synchrotron radiation, *Geophys. Res. Lett.*, *28*, 835-838, doi:10.1029/1999gl008446.
- Pei, S., and Y. Chen (2010), Tomographic structure of East Asia: I. No fast (slab) anomalies beneath 660 km discontinuity, *Earthq. Sci.*, *23*, 597-611, doi:10.1007/s11589-010-0759-X.
- Ribe, N. M., E. Stutzmann, Y. Ren, and R. van der Hilst (2007), Buckling instabilities of subducted lithosphere beneath the transition zone, *Earth Planet. Sci. Lett.*, *254*, 173-179, doi:10.1016/j.epsl.2006.11.028.
- Ringwood, A. E. (1982), Phase transformations and differentiation in subducted lithosphere: Implications for mantle dynamics, basalt petrogenesis, and crustal evolution, *J. Geol.*, *90*, 611-643.
- Ringwood, A. E., and T. Irifune (1988), Nature of the 650-km seismic discontinuity: Implications for mantle dynamics and differentiation, *Nature*, *331*, 131-136, doi:10.1038/331131a0.
- Ritsema, J., P. Cupillard, B. Tauzin, W. B. Xu, L. Stixrude, and C. Lithgow-Bertelloni (2009), Joint mineral physics and seismic wave traveltimes analysis of upper mantle temperature, *Geology*, *37*, 363-366, doi:10.1130/g25428a.1.
- Sanhira, T., T. Irifune, T. Shinmei, H. Ohfuji, F. Brunet, and K.-I. Funakoshi (2008), Density profiles of pyrolyte and MORB compositions across the 660-km seismic discontinuity, *High Pressure Res.*, *28*, 335-349, doi:10.1080/08957950802251357.
- Sawamoto, H. (1987), Phase diagram of MgSiO₃ at pressures up to 24 GPa and temperatures up to 2200°C: phase stability and properties of tetragonal garnet, in *High-Pressure Research in Mineral Physics: A Volume in Honor of Syun-iti Akimoto*, Geophys. Monogr. Ser., vol. 39, edited by M. H. Manghni and Y. Syono, pp. 209-219, AGU, Washington, D. C.
- Schmid, C., S. Goes, S. van der Lee, and D. Giardini (2002), Fate of the Cenozoic Farallon slab from a comparison of kinematic thermal modeling with tomographic images, *Earth Planet. Sci. Lett.*, *204*, 17-32, doi:10.1016/S0012-821X(02)00985-8.
- Shen, Y., and J. Blum (2003), Seismic evidence for accumulated oceanic crust above the 660-km discontinuity beneath southern Africa, *Geophys. Res. Lett.*, *30*, 1925, doi:10.1029/2003gl017991.

- Sinogeikin, S. V., and J. D. Bass (2002), Elasticity of pyrope and majorite-pyrope solid solutions to high temperatures, *Earth Planet. Sci. Lett.*, *203*, 549-555, doi:10.1016/S0012-821X(02)00851-8.
- Sinogeikin, S. V., J. D. Bass, and T. Katsura (2003), Single-crystal elasticity of ringwoodite to high pressures and high temperatures: Implications for 520 km seismic discontinuity, *Phys. Earth Planet. Inter.*, *136*, 41-66, doi:10.1016/S0031-9201(03)00022-0.
- Stähler S. C., K. Sigloch, and T. Nissen-Meyer (2012) Triplicated P-wave measurements for waveform tomography of the mantle transition zone, *Solid Earth*, *3*, 339-354, doi:10.5194/se-3-339-2012.
- Suzuki, A., E. Ohtani, H. Morishima, T. Kubo, Y. Kanbe, T. Kondo, T. Okada, H. Terasaki, T. Kato, and T. Kikegawa (2000), In situ determination of the phase boundary between wadsleyite and ringwoodite in Mg_2SiO_4 , *Geophys. Res. Lett.*, *27*, 803-806, doi:10.1029/1999gl008425.
- Tajima, F., I. Katayama, and T. Nakagawa (2009), Variable seismic structure near the 660 km discontinuity associated with stagnant slabs and geochemical implications, *Phys. Earth Planet. Inter.*, *172*, 183-198, doi:10.1016/j.pepi.2008.09.013.
- Tomioka, N., and K. Fujino (1999), Akimotoite, $(Mg,Fe)SiO_3$, a new silicate mineral of the ilmenite group in the Tenham chondrite, *Am. Mineral.*, *84*, 267-271.
- van der Hilst, R., R. Engdahl, W. Spakman, and G. Nolet (1991), Tomographic imaging of subducted lithosphere below northwest Pacific island arcs, *Nature*, *353*, 37-43, doi:10.1038/353037a0.
- Wang, C., Z. Jin, S. Gao, J. Zhang, and S. Zheng (2010), Eclogite-melt/peridotite reaction: Experimental constraints on the destruction mechanism of the North China Craton, *Sci. China Ser. D-Earth Sci.*, *53*, 797-809, doi:10.1007/s11430-010-3084-2.
- Watt, J. P., G. F. Davies, and R. J. O'Connell (1976), The elastic properties of composite materials, *Rev. Geophys.*, *14*, 541-563, doi:10.1029/RG014i004p00541.
- Wang, B., and F. Niu (2010), A broad 660 km discontinuity beneath northeast China revealed by dense regional seismic networks in China, *J. Geophys. Res.*, *115*, B06308, doi:10.1029/2009jb006608.
- Wang, T., and L. Chen (2009), Distinct velocity variations around the base of the upper mantle beneath northeast Asia, *Phys. Earth Planet. Inter.*, *172*, 241-256, doi:10.1016/j.pepi.2008.09.021.
- Wang, Y., D. J. Weidner, J. Zhang, G. D. Gwanmesia, and R. C. Liebermann (1998), Thermal equation of state of garnets along the pyrope-majorite join, *Phys. Earth Planet. Inter.*, *105*, 59-71, doi:10.1016/S0031-9201(97)00072-1.
- Wang, Y., D. J. Weidner, R. C. Liebermann, and Y. Zhao (1994), P-V-T equation of state of $(Mg,Fe)SiO_3$ perovskite: Constraints on composition of the lower mantle, *Phys. Earth Planet. Inter.*, *83*, 13-40, doi:10.1016/0031-9201(94)90109-0.
- Wang, Y., T. Uchida, J. Zhang, M. L. Rivers, and S. R. Sutton (2004), Thermal equation of state of akimotoite $MgSiO_3$ and effects of the akimotoite-garnet transformation on seismic structure near the 660 km discontinuity, *Phys. Earth Planet. Inter.*, *143-144*, 57-80, doi:10.1016/j.pepi.2003.08.007.
- Weidner, D. J., and E. Ito (1985), Elasticity of $MgSiO_3$ in the ilmenite phase, *Phys. Earth Planet. Inter.*, *40*, 65-70, doi:10.1016/0031-9201(85)90006-8.
- Weidner, D. J., and Y. Wang (2000), Phase transformations: Implications for mantle structure, in *Earth's Deep Interior: Mineral Physics and Tomography from the Atomic to the Global Scale*, Geophys. Monogr. Ser., vol. 117, edited by S. Karato, A. M. Forte, R. C. Liebermann, G. Masters and L. Stixrude, pp.117-235, AGU, Washington, D. C.
- Woodland, A. B., and R. J. Angel (1997), Reversal of the orthoferrosilite-high-P clinoferrosilite transition: a phase diagram for $FeSiO_3$ and implications for the mineralogy of the Earth's upper mantle, *Eur. J. Mineral.*, *9*, 245-254.
- Wu, Y., Y. B. Wang, Y. F. Zhang, Z. M. Jin, C. Wang, and C. Y. Zhou (2011), An experimental study of phase transformations in olivine under pressure and temperature conditions corresponding to the mantle transition zone, *Chinese Sci. Bull.*, doi:10.1007/s11434-011-4884-2.
- Xu, W., C. Lithgow-Bertelloni, L. Stixrude, and J. Ritsema (2008), The effect of bulk composition and temperature on mantle seismic structure, *Earth Planet. Sci. Lett.*, *275*, 70-79, doi:10.1016/j.epsl.2008.08.012.
- Yamazaki, D., T. Yoshino, T. Matsuzaki, T. Katsura, and A. Yoneda (2009), Texture of $(Mg,Fe)SiO_3$ perovskite and ferro-periclase aggregate: Implications for rheology of the lower mantle, *Phys. Earth Planet. Inter.*, *174*, 138-144, doi:10.1016/j.pepi.2008.11.002.
- Yoshioka, S., and A. Naganoda (2010), Effects of trench migration on fall of stagnant slabs into the lower mantle, *Phys. Earth Planet. Inter.*, *183*, 321-329, doi:10.1016/j.pepi.2010.09.002.
- Zha, C. S., T. S. Duffy, R. T. Downs, H. K. Mao, and R. J. Hemley (1998), Brillouin scattering and X-ray diffraction of San Carlos olivine: Direct pressure determination to 32 GPa, *Earth Planet. Sci. Lett.*, *159*, 25-33, doi:10.1016/S0012-821X(98)00063-6.
- Zhang, J., B. Li, W. Utsumi, and R. C. Liebermann (1996), In situ X-ray observations of the coesite-stishovite transition: reversed phase boundary and kinetics, *Phys. Chem. Miner.*, *23*, 1-10, doi:10.1007/bf00202987.
- Zhao, D. (2004), Global tomographic images of mantle plumes and subducting slabs: Insight into deep Earth dynamics, *Phys. Earth Planet. Inter.*, *146*, 3-34, doi:10.1016/j.pepi.2003.07.032.
- Zhao, D., Y. Tian, J. Lei, L. Liu, and S. Zheng (2009), Seismic image and origin of the Changbai intraplate volcano in East Asia: Role of big mantle wedge above the stagnant Pacific slab, *Phys. Earth Planet. Inter.*, *173*, 197-206, doi:10.1016/j.pepi.2008.11.009.
- Zhou, C., N. Nishiyama, T. Irifune, Y. Higo, and K. I. Funakoshi (2011), Equation of state and ultrasonic measurement of $MgSiO_3$ akimotoite at high pressures, *Eos Trans. AGU, Fall Meet. Suppl.*, Abstract MR41-A-2089.